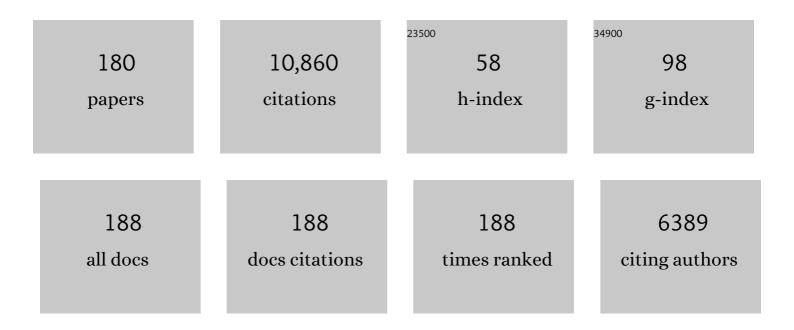
Chris G Ryan

List of Publications by Year in descending order

Source: https://exaly.com/author-pdf/8565605/publications.pdf Version: 2024-02-01



CHDIS C. RVAN

#	Article	IF	CITATIONS
1	SNIP, a statistics-sensitive background treatment for the quantitative analysis of PIXE spectra in geoscience applications. Nuclear Instruments & Methods in Physics Research B, 1988, 34, 396-402.	0.6	394
2	Quantitative trace element imaging using PIXE and the nuclear microprobe. International Journal of Imaging Systems and Technology, 2000, 11, 219-230.	2.7	337
3	Quantitative pixe microanalysis of geological matemal using the CSIRO proton microprobe. Nuclear Instruments & Methods in Physics Research B, 1990, 47, 55-71.	0.6	285
4	Dynamic analysis: on-line quantitative PIXE microanalysis and its use in overlap-resolved elemental mapping. Nuclear Instruments & Methods in Physics Research B, 1993, 77, 203-214.	0.6	259
5	Segregation of ore metals between magmatic brine and vapor; a fluid inclusion study using PIXE microanalysis. Economic Geology, 1992, 87, 1566-1583.	1.8	251
6	The evolution of lithospheric mantle beneath the Kalahari Craton and its margins. Lithos, 2003, 71, 215-241.	0.6	241
7	Layered Mantle Lithosphere in the Lac de Gras Area, Slave Craton: Composition, Structure and Origin. Journal of Petrology, 1999, 40, 705-727.	1.1	235
8	Harzburgite to lherzolite and back again: metasomatic processes in ultramafic xenoliths from the Wesselton kimberlite, Kimberley, South Africa. Contributions To Mineralogy and Petrology, 1999, 134, 232-250.	1.2	231
9	Garnet geotherms: Pressure-temperature data from Cr-pyrope garnet xenocrysts in volcanic rocks. Journal of Geophysical Research, 1996, 101, 5611-5625.	3.3	217
10	The Siberian lithosphere traverse: mantle terranes and the assembly of the Siberian Craton. Tectonophysics, 1999, 310, 1-35.	0.9	212
11	The X-ray Fluorescence Microscopy Beamline at the Australian Synchrotron. AIP Conference Proceedings, 2011, , .	0.3	208
12	Stable pit formation on AA2024-T3 in a NaCl environment. Corrosion Science, 2010, 52, 90-103.	3.0	181
13	Proton microprobe-determined partitioning of Nb, Ta, Zr, Sr and Y between garnet, clinopyroxene and basaltic magma at high pressure and temperature. Chemical Geology, 1989, 74, 201-216.	1.4	177
14	Elemental X-ray imaging using the Maia detector array: The benefits and challenges of large solid-angle. Nuclear Instruments and Methods in Physics Research, Section A: Accelerators, Spectrometers, Detectors and Associated Equipment, 2010, 619, 37-43.	0.7	176
15	A new method for on-line true-elemental imaging using PIXE and the proton microprobe. Nuclear Instruments & Methods in Physics Research B, 1995, 104, 157-165.	0.6	170
16	Residence of trace elements in metasomatized spinel lherzolite xenoliths: a proton-microprobe study. Contributions To Mineralogy and Petrology, 1991, 109, 98-113.	1.2	169
17	Corrosion of AA2024-T3 Part II: Co-operative corrosion. Corrosion Science, 2011, 53, 27-39.	3.0	169
18	Maia X-ray fluorescence imaging: Capturing detail in complex natural samples. Journal of Physics: Conference Series, 2014, 499, 012002.	0.3	162

#	Article	IF	CITATIONS
19	Trace elements in indicator minerals: area selection and target evaluation in diamond exploration. Journal of Geochemical Exploration, 1995, 53, 311-337.	1.5	157
20	Mineral inclusions in diamonds from the Sputnik kimberlite pipe, Yakutia. Lithos, 1997, 39, 135-157.	0.6	156
21	Composition and evolution of ore fluids in a magmatic-hydrothermal skarn deposit. Geology, 2004, 32, 117.	2.0	156
22	Laser-ablation microprobe (LAM)-ICPMS unravels the highly siderophile element geochemistry of the oceanic mantle. Earth and Planetary Science Letters, 2001, 189, 285-294.	1.8	144
23	Melt Inclusions in Veins: Linking Magmas and Porphyry Cu Deposits. Science, 2003, 302, 2109-2111.	6.0	137
24	Quantitative analysis of PIXE spectra in geoscience applications. Nuclear Instruments & Methods in Physics Research B, 1990, 49, 271-276.	0.6	135
25	Megapixel imaging of (micro)nutrients in mature barley grains. Journal of Experimental Botany, 2011, 62, 273-282.	2.4	134
26	Ni in chrome pyrope garnets: a new geothermometer. Contributions To Mineralogy and Petrology, 1989, 103, 199-202.	1.2	130
27	In Situ Distribution and Speciation of Toxic Copper, Nickel, and Zinc in Hydrated Roots of Cowpea Â. Plant Physiology, 2011, 156, 663-673.	2.3	130
28	Nuclear microprobe – synchrotron synergy: Towards integrated quantitative real-time elemental imaging using PIXE and SXRF. Nuclear Instruments & Methods in Physics Research B, 2005, 231, 183-188.	0.6	129
29	Natural gold particles in Eucalyptus leaves and their relevance to exploration for buried gold deposits. Nature Communications, 2013, 4, 2614.	5.8	122
30	Trace-element zoning in garnets from sheared mantle xenoliths. Geochimica Et Cosmochimica Acta, 1989, 53, 561-567.	1.6	114
31	Determination of the oxidation state of Cu in substituted Cu-In-Fe-bearing sphalerite via Â-XANES spectroscopy. American Mineralogist, 2012, 97, 476-479.	0.9	114
32	Developments in Dynamic Analysis for quantitative PIXE true elemental imaging. Nuclear Instruments & Methods in Physics Research B, 2001, 181, 170-179.	0.6	113
33	Trace elements in sulfide inclusions from Yakutian diamonds. Contributions To Mineralogy and Petrology, 1996, 124, 111-125.	1.2	107
34	Xâ€ray elemental mapping techniques for elucidating the ecophysiology of hyperaccumulator plants. New Phytologist, 2018, 218, 432-452.	3.5	104
35	Trace elements in garnets and chromites: Diamond formation in the Siberian lithosphere. Lithos, 1993, 29, 235-256.	0.6	102
36	The NAC nuclear microprobe facility. Nuclear Instruments & Methods in Physics Research B, 1995, 104, 36-42.	0.6	100

#	Article	IF	CITATIONS
37	The partitioning of Fe, Ni, Cu, Pt, and Au between sulfide, metal, and fluid phases: A pilot study. Geochimica Et Cosmochimica Acta, 1994, 58, 811-826.	1.6	93
38	Trends in hard X-ray fluorescence mapping: environmental applications in the age of fast detectors. Analytical and Bioanalytical Chemistry, 2011, 400, 1637-1644.	1.9	93
39	Conditions of diamond growth: a proton microprobe study of inclusions in West Australian diamonds. Contributions To Mineralogy and Petrology, 1988, 99, 143-158.	1.2	90
40	Variations in trapping temperatures and trace elements in peridotite-suite inclusions from African diamonds: evidence for two inclusion suites, and implications for lithosphere stratigraphy. Contributions To Mineralogy and Petrology, 1992, 110, 1-15.	1.2	89
41	The New Maia Detector System: Methods For High Definition Trace Element Imaging Of Natural Material. AIP Conference Proceedings, 2010, , .	0.3	89
42	Fast X-Ray Fluorescence Microtomography of Hydrated Biological Samples. PLoS ONE, 2011, 6, e20626.	1.1	89
43	Trace element geochemistry of ilmenite megacrysts from the Monastery kimberlite, South Africa. Lithos, 1992, 29, 1-18.	0.6	83
44	Nucleation environment of diamonds from Yakutian kimberlites. Mineralogical Magazine, 1998, 62, 409-419.	0.6	82
45	Laterally resolved speciation of arsenic in roots of wheat and rice using fluorescenceâ€ <scp>XANES</scp> imaging. New Phytologist, 2014, 201, 1251-1262.	3.5	81
46	High-Definition X-ray Fluorescence Elemental Mapping of Paintings. Analytical Chemistry, 2012, 84, 3278-3286.	3.2	79
47	Maia X-ray Microprobe Detector Array System. Journal of Physics: Conference Series, 2014, 499, 012001.	0.3	78
48	Trace element partitioning between aqueous fluids, silicate melts and minerals. European Journal of Mineralogy, 1997, 9, 569-584.	0.4	76
49	The XFM beamline at the Australian Synchrotron. Journal of Synchrotron Radiation, 2020, 27, 1447-1458.	1.0	75
50	Thermal state and composition of the lithospheric mantle beneath the Daldyn kimberlite field, Yakutia. Tectonophysics, 1996, 262, 19-33.	0.9	73
51	Immiscibility between silicate magmas and aqueous fluids: a melt inclusion pursuit into the magmatic-hydrothermal transition in the Omsukchan Granite (NE Russia). Chemical Geology, 2004, 210, 73-90.	1.4	72
52	Trace-element zonation in garnets from The Thumb: heating and melt infiltration below the Colorado Plateau. Contributions To Mineralogy and Petrology, 1991, 107, 60-79.	1.2	66
53	Cr-pyrope garnets in the lithospheric mantle 2. Compositional populations and their distribution in time and space. Geochemistry, Geophysics, Geosystems, 2002, 3, 1-35.	1.0	64
54	Quantitative PIXE microanalysis of fluid inclusions based on a layered yield model. Nuclear Instruments & Methods in Physics Research B, 1991, 54, 292-297.	0.6	63

#	Article	IF	CITATIONS
55	Subduction signature for quenched carbonatites from the deep lithosphere. Geology, 2002, 30, 743.	2.0	61
56	X-ray nanoprobes and diffraction-limited storage rings: opportunities and challenges of fluorescence tomography of biological specimens. Journal of Synchrotron Radiation, 2014, 21, 1031-1047.	1.0	61
57	The new CSIRO–GEMOC nuclear microprobe: First results, performance and recent applications. Nuclear Instruments & Methods in Physics Research B, 2001, 181, 12-19.	0.6	60
58	Probing ore deposits formation: New insights and challenges from synchrotron and neutron studies. Radiation Physics and Chemistry, 2010, 79, 151-161.	1.4	58
59	Melt inclusions from the deep Slave lithosphere: implications for the origin and evolution of mantle-derived carbonatite and kimberlite. Lithos, 2004, 76, 461-474.	0.6	56
60	Extreme chemical heterogeneity of granite-derived hydrothermal fluids: An example from inclusions in a single crystal of miarolitic quartz. Geology, 2002, 30, 459.	2.0	55
61	Speciation mapping of environmental samples using XANES imaging. Environmental Chemistry, 2014, 11, 341.	0.7	55
62	Quantitative comparison of preparation methodologies for x-ray fluorescence microscopy of brain tissue. Analytical and Bioanalytical Chemistry, 2011, 401, 853-864.	1.9	53
63	Lifetimes of excited states in 196, 198Pt; Application of interacting boson approximation model to even Pt isotopes systematics. Nuclear Physics A, 1981, 370, 146-174.	0.6	52
64	Mixed messages in iron oxide–copper–gold systems of the Cloncurry district, Australia: insights from PIXE analysis of halogens and copper in fluid inclusions. Mineralium Deposita, 2008, 43, 599-608.	1.7	52
65	Reduced As components in highly oxidized environments: Evidence from full spectral XANES imaging using the Maia massively parallel detector. American Mineralogist, 2010, 95, 884-887.	0.9	52
66	A multi-technique investigation of copper and zinc distribution, speciation and potential bioavailability in biosolids. Environmental Pollution, 2012, 166, 57-64.	3.7	52
67	The nuclear microprobe as a tool in geology and mineral exploration. Nuclear Instruments & Methods in Physics Research B, 1993, 77, 381-398.	0.6	51
68	An electrostatic "Russian―quadruplet microprobe lens. Nuclear Instruments & Methods in Physics Research B, 1986, 15, 664-668.	0.6	50
69	Compositional evolution of high-temperature sheared lherzolite PHN 1611. Geochimica Et Cosmochimica Acta, 1993, 57, 605-613.	1.6	50
70	Fast X-ray microfluorescence imaging with submicrometer-resolution integrating a Maia detector at beamline P06 at PETRAâ€III. Journal of Synchrotron Radiation, 2016, 23, 1550-1560.	1.0	49
71	The impact of steeping, germination and hydrothermal processing of wheat (Triticum aestivum L.) grains on phytate hydrolysis and the distribution, speciation and bio-accessibility of iron and zinc elements. Food Chemistry, 2018, 264, 367-376.	4.2	49
72	Quantified, multi-scale X-ray fluorescence element mapping using the Maia detector array: application to mineral deposit studies. Mineralium Deposita, 2015, 50, 665-674.	1.7	48

#	Article	IF	CITATIONS
73	Caenorhabditis elegans Maintains Highly Compartmentalized Cellular Distribution of Metals and Steep Concentration Gradients of Manganese. PLoS ONE, 2012, 7, e32685.	1.1	47
74	A high performance quadrupole quintuplet lens system for the CSIRO–GEMOC nuclear microprobe. Nuclear Instruments & Methods in Physics Research B, 1999, 158, 97-106.	0.6	44
75	PIXE and the nuclear microprobe: Tools for quantitative imaging of complex natural materials. Nuclear Instruments & Methods in Physics Research B, 2011, 269, 2151-2162.	0.6	44
76	Gyromagnetic ratios of excited states in 198Pt; measurements and interacting boson approximation model calculations. Nuclear Physics A, 1981, 365, 317-332.	0.6	43
77	Trace elements in tourmalines from massive sulfides deposits and tourmalinites; geochemical controls and exploration applications. Economic Geology, 1996, 91, 657-675.	1.8	43
78	Evolution and source of ore fluids in the stringer system, Hellyer VHMS deposit, Tasmania, Australia: evidence from fluid inclusion microthermometry and geochemistry. Ore Geology Reviews, 1996, 10, 251-278.	1.1	41
79	Full spectral XANES imaging using the Maia detector array as a new tool for the study of the alteration process of chrome yellow pigments in paintings by Vincent van Gogh. Journal of Analytical Atomic Spectrometry, 2015, 30, 613-626.	1.6	40
80	Correlation between Chemical and Morphological Heterogeneities in LiNi _{0.5} Mn _{1.5} O ₄ Spinel Composite Electrodes for Lithium-Ion Batteries Determined by Micro-X-ray Fluorescence Analysis. Chemistry of Materials, 2015, 27, 2525-2531.	3.2	40
81	In situ analysis of Refractory Metal Nuggets in carbonaceous chondrites. Geochimica Et Cosmochimica Acta, 2017, 216, 61-81.	1.6	40
82	Microanalysis of ore-forming fluids using the scanning proton microprobe. Nuclear Instruments & Methods in Physics Research B, 1995, 104, 182-190.	0.6	39
83	Imaging with ionoluminescence (IL) in a nuclear microprobe. Nuclear Instruments & Methods in Physics Research B, 1993, 77, 188-194.	0.6	38
84	Quantitative determination of metal and metalloid spatial distribution in hydrated and fresh roots of cowpea using synchrotron-based X-ray fluorescence microscopy. Science of the Total Environment, 2013, 463-464, 131-139.	3.9	38
85	Arsenic in hydrothermal apatite: Oxidation state, mechanism of uptake, and comparison between experiments and nature. Geochimica Et Cosmochimica Acta, 2017, 196, 144-159.	1.6	38
86	Contrasts in gem corundum characteristics, eastern Australian basaltic fields: trace elements, fluid/melt inclusions and oxygen isotopes. Mineralogical Magazine, 2006, 70, 669-687.	0.6	37
87	Distribution of Metals in the Termite Tumulitermes tumuli (Froggatt): Two Types of Malpighian Tubule Concretion Host Zn and Ca Mutually Exclusively. PLoS ONE, 2011, 6, e27578.	1.1	37
88	Extremely Ni-rich Fe–Ni sulfide assemblages in komatiitic dunite at Betheno, Western Australia: results from synchrotron X-ray fluorescence mapping. Australian Journal of Earth Sciences, 2011, 58, 691-709.	0.4	37
89	GEOCHEMISTRY OF HYPERSALINE FLUID INCLUSIONS FROM THE STARRA (Fe OXIDE)-Au-Cu DEPOSIT, CLONCURRY DISTRICT, QUEENSLAND. Economic Geology, 2001, 96, 875-883.	1.8	37
90	Microthermometry and chemical composition of fluid inclusions from the Mt Chalmers volcanic-hosted massive sulfide deposits, central Queensland, Australia: implications for ore genesis. Chemical Geology, 2003, 194, 225-244.	1.4	34

#	Article	IF	CITATIONS
91	Large detector array and real-time processing and elemental image projection of X-ray and proton microprobe fluorescence data. Nuclear Instruments & Methods in Physics Research B, 2007, 260, 1-7.	0.6	34
92	Disparity between the transient hyperfine fields for Pt and Os in Fe; an electron vacancy sharing interpretation. Hyperfine Interactions, 1983, 13, 275-295.	0.2	33
93	Imaging fluid inclusion content using the new CSIRO–GEMOC nuclear microprobe. Nuclear Instruments & Methods in Physics Research B, 2001, 181, 570-577.	0.6	33
94	Geological controls on refractory ore in an orogenic gold deposit, Macraes mine, New Zealand. Mineralium Deposita, 2005, 40, 45-58.	1.7	33
95	Carbonate Replacement as the Principal Ore Formation Process in the Proterozoic McArthur River (HYC) Sediment-Hosted Zn-Pb Deposit, Australia. Economic Geology, 2021, 116, 693-718.	1.8	33
96	The use of spectroscopic imaging and mapping techniques in the characterisation and study of DLD-1 cell spheroid tumour models. Integrative Biology (United Kingdom), 2012, 4, 1072-1080.	0.6	32
97	Ore Petrography Using Megapixel X-Ray Imaging: Rapid Insights into Element Distribution and Mobilization in Complex Pt and U-Ge-Cu Ores. Economic Geology, 2016, 111, 487-501.	1.8	32
98	Improved Dynamic Analysis method for quantitative PIXE and SXRF element imaging of complex materials. Nuclear Instruments & Methods in Physics Research B, 2015, 363, 42-47.	0.6	31
99	Maia Mapper: high definition XRF imaging in the lab. Journal of Instrumentation, 2018, 13, C03020-C03020.	0.5	31
100	Formation of the Denchai gem sapphires, northern Thailand: evidence from mineral chemistry and fluid/melt inclusion characteristics. Mineralogical Magazine, 2001, 65, 725-735.	0.6	30
101	Chemical fingerprinting of hydrothermal zircons: an example from the Gidginbung high sulphidation Au-Ag-(Cu) deposit, New South Wales, Australia. Proceedings of the Geologists Association, 2007, 118, 37-46.	0.6	29
102	The Maia 384 detector array in a nuclear microprobe: A platform for high definition PIXE elemental imaging. Nuclear Instruments & Methods in Physics Research B, 2010, 268, 1899-1902.	0.6	29
103	Primary cumulus platinum minerals in the Monts de Cristal Complex, Gabon: magmatic microenvironments inferred from high-definition X-ray fluorescence microscopy. Contributions To Mineralogy and Petrology, 2016, 171, 1.	1.2	29
104	Spiral scanning X-ray fluorescence computed tomography. Optics Express, 2017, 25, 23424.	1.7	28
105	Spatial Distribution of Lead in Enamel and Coronal Dentine of Wistar Rats. Biological Trace Element Research, 2005, 105, 159-170.	1.9	26
106	Ionic gold in calcrete revealed by LA-ICP-MS, SXRF and XANES. Geochimica Et Cosmochimica Acta, 2009, 73, 1666-1683.	1.6	26
107	Visualising coordination chemistry: fluorescence X-ray absorption near edge structure tomography. Chemical Communications, 2016, 52, 11834-11837.	2.2	26
108	Trace Element Mapping of Copper- and Zinc-Rich Black Smoker Chimneys from Brothers Volcano, Kermadec Arc, Using Synchrotron Radiation XFM and LA-ICP-MS. Economic Geology, 2019, 114, 67-92.	1.8	26

#	Article	IF	CITATIONS
109	PIXE profiling, imaging and analysis using the NAC proton microprobe: Unraveling mantle eclogites. Nuclear Instruments & Methods in Physics Research B, 1995, 104, 415-426.	0.6	24
110	Statistical techniques for the classification of chromites in diamond exploration samples. Journal of Geochemical Exploration, 1997, 59, 233-249.	1.5	24
111	Advances in Dynamic Analysis PIXE imaging: Correction for spatial variation of pile-up components. Nuclear Instruments & Methods in Physics Research B, 2005, 231, 162-169.	0.6	24
112	Release of uranium from highly radiogenic zircon through metamictization: The source of orogenic uranium ores. Geology, 2016, 44, 15-18.	2.0	24
113	The Maia Detector and Event Mode. Synchrotron Radiation News, 2018, 31, 21-27.	0.2	24
114	High-throughput X-ray fluorescence imaging using a massively parallel detector array, integrated scanning and real-time spectral deconvolution. Journal of Physics: Conference Series, 2009, 186, 012013.	0.3	23
115	Elemental and mineralogical study of earth-based pigments using particle induced X-ray emission and X-ray diffraction. Nuclear Instruments and Methods in Physics Research, Section A: Accelerators, Spectrometers, Detectors and Associated Equipment, 2010, 619, 306-310.	0.7	23
116	The CSIRO-GEMOC Nuclear Microprobe: a high-performance system based on a new closely integrated design. Nuclear Instruments & Methods in Physics Research B, 1999, 158, 18-23.	0.6	22
117	Ion beam microanalysis in geoscience research. Nuclear Instruments & Methods in Physics Research B, 2004, 219-220, 534-549.	0.6	22
118	The Maia detector array and x-ray fluorescence imaging system: locating rare precious metal phases in complex samples. Proceedings of SPIE, 2013, , .	0.8	22
119	Quantified, whole section trace element mapping of carbonaceous chondrites by Synchrotron X-ray Fluorescence Microscopy: 1. CV meteorites. Geochimica Et Cosmochimica Acta, 2014, 134, 100-119.	1.6	22
120	Advances in fluid inclusion analysis using the nuclear microprobe. Nuclear Instruments & Methods in Physics Research B, 1999, 158, 523-532.	0.6	19
121	Accumulation of transition metals and metalloids in sulfidized stromatolites of the 3.48 billion–year–old Dresser Formation, Pilbara Craton. Precambrian Research, 2020, 337, 105534.	1.2	19
122	A Labview based FPGA data acquisition with integrated stage and beam transport control. Nuclear Instruments & Methods in Physics Research B, 2013, 306, 71-75.	0.6	18
123	An experimental calibration of the "nickel in garnet" geothermometer with applications, by D. Canil: discussion. Contributions To Mineralogy and Petrology, 1996, 124, 216-218.	1.2	17
124	Geochemistry of Au-bearing pyrite from the Sepon Mineral District, Laos DPR, Southeast Asia: Implications for ore genesis. Journal of Asian Earth Sciences, 2018, 164, 194-218.	1.0	17
125	Gyromagnetic ratios of low-lying excited states inPt196. Physical Review C, 1981, 24, 2106-2113.	1.1	16
126	Lattice location of gold in natural pyrite crystals. Nuclear Instruments & Methods in Physics Research B, 1999, 152, 135-144.	0.6	16

#	Article	IF	CITATIONS
127	Applications of PIXE and diagnostic leaching in the characterisation of complex gold ores. Minerals Engineering, 2005, 18, 1010-1019.	1.8	16
128	Modeling outflow from the Ernest Henry Fe oxide Cu–Au deposit: implications for ore genesis and exploration. Journal of Geochemical Exploration, 2005, 85, 31-46.	1.5	16
129	Imaging trace-element zoning in pyroxenes using synchrotron XRF mapping with the Maia detector array: Benefit of low-incident energy. American Mineralogist, 2020, 105, 136-140.	0.9	16
130	Formation of microâ€spherulitic barite in association with organic matter within sulfidized stromatolites of the 3.48 billionâ€yearâ€old Dresser Formation, Pilbara Craton. Geobiology, 2020, 18, 415-425.	1.1	16
131	Variations of the gyromagnetic ratios of low-lying states in 192Os. Nuclear Physics A, 1983, 401, 175-188.	0.6	15
132	Combined nuclear microprobe and TEM study of corrosion pit nucleation by intermetallics in aerospace aluminium alloys. Nuclear Instruments & Methods in Physics Research B, 2005, 231, 457-462.	0.6	15
133	Synchrotron X-ray microscopy reveals early calcium and iron interaction with crocidolite fibers in the lung of exposed mice. Toxicology Letters, 2016, 241, 111-120.	0.4	15
134	Velocity dependence of the transient hyperfine field at Pd ions swiftly recoiling through magnetized Fe. Physical Review C, 1981, 23, 1618-1623.	1.1	14
135	PIXE-quantified AXSIA: Elemental mapping by multivariate spectral analysis. Nuclear Instruments & Methods in Physics Research B, 2006, 249, 828-832.	0.6	14
136	Particle Characterisation and Depletion of Li2CO3 Inhibitor in a Polyurethane Coating. Coatings, 2017, 7, 106.	1.2	14
137	Magmatic inclusions in the search for natural silicate-salt melt immiscibility: Methodology and examples. Developments in Volcanology, 2003, , 65-82.	0.5	13
138	Hyper-spectral ionoluminescence system for minerals and fluid inclusions. Nuclear Instruments & Methods in Physics Research B, 2011, 269, 2244-2250.	0.6	13
139	Velocity dependence of transient hyperfine field at Pt ions rapidly recoiling through magnetized Fe. Physical Review C, 1981, 24, 1480-1485.	1.1	12
140	The application of synchrotron radiation induced X-ray emission in the measurement of zinc and lead in Wistar rat ameloblasts. Archives of Oral Biology, 2007, 52, 938-944.	0.8	12
141	STIM evaluation in GeoPIXE to complement the quantitative dynamic analysis. Nuclear Instruments & Methods in Physics Research B, 2009, 267, 2080-2084.	0.6	12
142	Iron-rich particles in heavily contaminated multicrystalline silicon wafers and their response to phosphorus gettering. Semiconductor Science and Technology, 2012, 27, 125016.	1.0	12
143	Experimental studies on the gold-in-calcrete anomaly at Edoldeh Tank Gold Prospect, Gawler Craton, South Australia. Journal of Geochemical Exploration, 2012, 112, 189-205.	1.5	12
144	Simultaneous X-ray diffraction, crystallography and fluorescence mapping using the Maia detector. Acta Materialia, 2018, 144, 1-10.	3.8	12

#	Article	IF	CITATIONS
145	Fast XANES fluorescence imaging using a Maia detector. Journal of Synchrotron Radiation, 2018, 25, 892-898.	1.0	12
146	Rare earth elements, aluminium and silicon distribution in the fern <i>Dicranopteris linearis</i> revealed by 14/PIXE Maia analysis. Annals of Botany, 2021, 128, 17-30.	1.4	12
147	Mineralogical and Microchemical Methods for the Characterization of High-Grade Banded Iron Formation-Derived Iron Ore. , 2008, , .		11
148	Particle induced gamma and X-ray emission spectroscopies of lithium based alloy coatings. Nuclear Instruments & Methods in Physics Research B, 2017, 404, 167-172.	0.6	10
149	Life on the edge: Microbial biomineralization in an arsenic- and lead-rich deep-sea hydrothermal vent. Chemical Geology, 2020, 533, 119438.	1.4	10
150	Spatial Association Between Platinum Minerals and Magmatic Sulfides Imaged with the Maia Mapper and Implications for the Origin of the Chromite-Sulfide-PGE Association. Canadian Mineralogist, 2021, ,	0.3	10
151	Endosperm prevents toxic amounts of Zn from accumulating in the seed embryo – an adaptation to metalliferous sites in metal-tolerant <i>Biscutella laevigata</i> . Metallomics, 2020, 12, 42-53.	1.0	9
152	Transient hyperfine field measurements of gyromagnetic ratios in Os and Pt nuclei. Physical Review C, 1983, 27, 434-437.	1.1	8
153	Scanning Xâ€ray fluorescence microspectroscopy of metallic impurities in solarâ€grade silicon. Physica Status Solidi (A) Applications and Materials Science, 2010, 207, 1807-1810.	0.8	8
154	The Interplay of Evolved Seawater and Magmatic-Hydrothermal Fluids in the 3.24 Ga Panorama Volcanic-Hosted Massive Sulfide Hydrothermal System, North Pilbara Craton, Western Australia. Economic Geology, 2013, 108, 79-110.	1.8	8
155	Lattice location of nickel in diamond by RBS channelling and PIXE. Physica Status Solidi (A) Applications and Materials Science, 2011, 208, 42-46.	0.8	7
156	Leucostaurite, Pb2[B5O9]Cl{middle dot}0.5H2O, from the Atacama Desert: The first Pb-dominant member of the hilgardite group, and micro-determination of boron in minerals by PIGE. American Mineralogist, 2012, 97, 1206-1212.	0.9	7
157	Micron-scale distribution of metals in Cambrian metalliferous shales, South China: Insights into local biologically driven redox disequilibrium. Chemical Geology, 2019, 528, 119283.	1.4	7
158	Microelectronic junctions in arsenian pyrite due to impurity and mixed sulfide heterogeneity. American Mineralogist, 2015, 100, 26-34.	0.9	6
159	Next generation data acquisition systems for the CSIRO Nuclear Microprobe: Highly scaled versus customizable. Nuclear Instruments & Methods in Physics Research B, 2017, 404, 15-20.	0.6	6
160	PIXE imaging of hyperaccumulator plants using the Maia detector array. Nuclear Instruments & Methods in Physics Research B, 2019, 451, 73-78.	0.6	6
161	Level structure and lifetimes of low-excitation states in 63Cu. Nuclear Physics A, 1980, 342, 373-384.	0.6	5
162	Mapping elemental distributions in submarine hydrothermal sulfide smokers using proton induced X-ray emission. Nuclear Instruments & Methods in Physics Research B, 2010, 268, 2129-2132.	0.6	5

#	Article	IF	CITATIONS
163	Impurity mapping in sulphide minerals using Time-resolved Ion Beam Induced Current imaging. Nuclear Instruments & Methods in Physics Research B, 2010, 268, 1903-1910.	0.6	5
164	Validation of aGeant4model of the X-ray fluorescence microprobe at the Australian Synchrotron. Journal of Synchrotron Radiation, 2015, 22, 354-365.	1.0	5
165	Laser-beam-induced current microscopy of electric fields in natural minerals caused by impurity zonation and structural defects. Measurement Science and Technology, 2012, 23, 085401.	1.4	4
166	Polycrystalline materials analysis using the Maia pixelated energy-dispersive X-ray area detector. Powder Diffraction, 2017, 32, S16-S21.	0.4	4
167	Selective x-ray Bragg spectrometry: optimizing fluorescence microprobe sensitivity for precious metals. X-Ray Spectrometry, 2007, 36, 111-121.	0.9	3
168	The Maia Detector Journey: Development, Capabilities and Applications. Microscopy and Microanalysis, 2018, 24, 720-721.	0.2	3
169	Biogenicity of Spicular Geyserite from Te Kopia, New Zealand: Integrated Petrography, High-Resolution Hyperspectral and Elemental Analysis. Astrobiology, 2021, 21, 115-135.	1.5	3
170	Phase correlations of elemental maps using nuclear microscopy. Nuclear Instruments & Methods in Physics Research B, 2003, 210, 129-134.	0.6	2
171	Lead and zinc-rich fluid inclusions in Broken Hill-type deposits: Fractionates from sulphide-rich melts or consequences of exotic fluid infiltration?. , 2005, , 861-864.		2
172	High definition large area mapping of geological samples using a Maia detector array in the Nuclear Microprobe. Nuclear Instruments & Methods in Physics Research B, 2019, 449, 11-16.	0.6	2
173	Recoil-distance Lifetime Measurements of 47SC Levels. Australian Journal of Physics, 1982, 35, 371.	0.6	2
174	Fluid inclusion and stable isotope geochemistry of the Ernest Henry Fe oxide-Cu-Au deposit, Queensland, Australia. , 2005, , 785-788.		1
175	High-definition mapping of trace metal elements in the hippocampus in a model of closed-head traumatic brain injury. Injury, 2010, 41, S30-S31.	0.7	1
176	Impurity heterogeneity in natural pyrite and its relation to internal electric fields mapped using remote laser beam induced current. Nuclear Instruments & Methods in Physics Research B, 2013, 306, 249-252.	0.6	1
177	Maia Mapper: High Definition XRF Imaging of Geological Samples at Intermediate Spatial Scales. Microscopy and Microanalysis, 2018, 24, 110-111.	0.2	1
178	Evidence supporting micro-galvanic coupling in sulphides leads to gold deposition. Contributions To Mineralogy and Petrology, 2021, 176, 1.	1.2	1
179	Application of Nuclear Microprobes towards Understanding Complex Ore Geo-electrochemistry. EPJ Web of Conferences, 2012, 35, 02002.	0.1	0
180	Biomolecular modifications in the sacfry of Mogurnda adspersa in response to copper stress. Aquatic Toxicology, 2022, 248, 106179.	1.9	0